First Principles Calculation of a Large Variation in Dielectric Tensor Through the Spin Crossover in the $CsFe[Cr(CN)_6]$ Prussian Blue Analogue

Derek S. Middlemiss and Robert J. Deeth

Inorganic Computational Chemistry Group,

Department of Chemistry, University of Warwick,

Coventry, CV4 7AL, UK

E-mail: derekmiddlemiss@gmail.com and

R.J.Deeth@warwick.ac.uk

Abstract

The dielectric response of spin-crossover (SCO) materials is a key property facilitating their use in next-generation information processing technologies. Solid state hybrid density functional theory calculations show that the temperature-induced and strongly hysteretic SCO transition in the $Cs^{+}Fe^{2+}[Cr^{3+}(CN^{-})_6]$ Prussian blue analogue is associated with a large change (Δ) in both the static, $\Delta\varepsilon^{0}(\mathrm{HS}-\mathrm{LS})$, and high frequency, $\Delta\varepsilon^{\infty}(\mathrm{HS}-\mathrm{LS})$ dielectric constants. The SCO-induced variation in $CsFe[Cr(CN)_6]$ is significantly greater than the experimental $\Delta\varepsilon$ values observed previously in other SCO materials. The phonon contribution, $\Delta\varepsilon^{\mathrm{phon}}(\mathrm{HS}-\mathrm{LS})$, determined within a lattice dynamics approach, dominates over the clamped nuclei term, $\Delta\varepsilon^{\infty}(\mathrm{HS}-\mathrm{LS})$, and is in turn dominated by the low-frequency translational motions of Cs^{+} cations within the cubic voids of the $Fe[Cr(CN)_6]^{-}$ framework. The Cs^{+} translational modes couple strongly to the large unit cell volume change occurring through the SCO transition. PBAs and associated metal-organic frameworks emerge as a potentially fruitful class of materials in which to search for SCO transitions associated with large changes in dielectric response and other macroscopic properties.

Keywords

spin crossover materials, bistability, dielectric properties, density functional theory, phonons, lattice dynamics, solid-state

I. Introduction

Spin crossover (SCO) is a technologically relevant phenomenon in compounds bearing transition metals (TMs). It is most commonly observed in octahedral d^4 through d^7 complexes, especially six-fold coordinated Fe(II) species [1,2]. The thermal SCO transition from the low spin (LS) to the high spin (HS) state of the TM species [i.e. $^1A_{1g}$ to $^5T_{2g}$ for octahedral Fe(II)], and vice-versa, is characterized by the spin transition temperature, $T_{1/2}$, corresponding to the temperature at which half the SCO-active complexes or sites are in their HS state and half are LS. SCO can be induced by application of a variety of external perturbations, including variations in temperature or pressure, visible light and X-ray irradiation, static electric and magnetic fields, and absorption or desorption of guest molecules into the lattice [3-10].

Solid-state SCO compounds are of particular interest for a number of reasons. Firstly, they often display bistability, in that $T_{1/2}$ depends on whether the sample is being heated ($\uparrow$) or cooled ($\downarrow$) through the transition. The hysteretic temperature range $T_{1/2}(\uparrow) - T_{1/2}(\downarrow)$ is strongly lattice-dependent. It is mediated and controlled by the elastic interactions between SCO-active centers in the crystal structure [11-14], and should be controllable by a process of rational materials design and synthesis [15-17]. Secondly, SCO transitions are often accompanied by readily detectable changes in related properties of the materials, most obviously the magnetic susceptibility [18-20], but also, for example, the crystal and molecular structures [21-25], the infrared (IR), Raman and nuclear inelastic scattering vibrational spectra [26-28], the Mössbauer spectra [29,30], the optical excitation spectra (often leading to a color change)

[31,32], the electrical conductivity [33-35], and, of particular relevance here, the dielectric tensor governing the polarization response of the material to applied electric fields [36-39]. The combination of molecular bistability with detectable response properties has led to suggestions that SCO materials might be applied as switching elements in next generation information processing and display technologies [6,40,41] and in novel gas sensors [10,42]. Efforts persist to synthesize materials with broad SCO hysteresis widths centered at equilibrium temperature [15,43,44]. The light-induced excited spin state trapping (LIESST) phenomenon also opens up the useful possibility of the optical addressing of SCO-active elements in such technologies, and efforts are ongoing to synthesize materials showing increased limiting temperatures, T_{LIESST}, associated with this effect [45-47].

SCO-induced variations in dielectric tensor are potentially very relevant to new information processing technologies, for they offer the possibility of a purely electronic readout of the state of an SCO-active element, likely based upon a straightforward capacitive measurement [48]. Previous studies of the dielectric parameters of SCO materials are somewhat rare in the literature. Bousseksou *et al.* have reported a comprehensive study of the dielectric properties of SCO solids by application of dynamic dielectric spectroscopy (DDS), providing the isothermal frequency dependent dielectric constant, $\varepsilon(\nu)$. A range of Fe^{2+} complexes were studied exhibiting varying types of SCO transitions with $T_{1/2}$ in the range 130−330 K. In general, it was observed that the $\varepsilon(T)$-temperature (T) curves accurately tracked the HS state site fraction $\gamma(T)$ curves derived from susceptibility or optical reflectivity measurements, the $\Delta\varepsilon(HS-LS)$ (denoted $\Delta\varepsilon$ hereafter) values falling in the range −0.07 to +0.3 and being positive in the majority of materials [36].

Guillon *et al.* later studied $\varepsilon(T)$ in the $[Fe(bpp)_2](BF_4)_2$ SCO complex (where bpp = 2,6-*bis*{pyrazol-3-yl}pyridine) using DDS, and also performed isolated molecule density functional theory (DFT) calculations at the B3LYP/6-31G* level, seeking to correlate the computed difference in HS and LS state polarizabilities, $\Delta\alpha(HS-LS)$ = +7.01 atomic units ($\Delta\alpha$ and AU hereafter), with the experimental $\Delta\varepsilon$ value at −0.11. The fact that $\Delta\alpha$ and $\Delta\varepsilon$ are of opposite sign was attributed to the neglect of the $[BF_4]^-$ counter-anions in the calculations [37]. Bonhommeau *et al.* demonstrated in 2006 that photoswitching in the $[Fe(L)(CN)_2]\cdot H_2O$ complex (where L is a large Schiff base macrocyclic ligand) at a temperature below T_{LIESST} = 130 K is associated with a detectable change in dielectric constant. The experimental $\Delta\varepsilon$ and DFT computed (B3LYP/6-31G*) $\Delta\alpha$ values for the title and two further complexes generally agreed in sign, if not in relative magnitudes. The maximum $\Delta\varepsilon$ value observed was +0.18 for the title complex [38]. Terahertz time domain spectroscopy [49] and spectroscopic ellipsometry [50] have also been used to probe SCO materials, both methods revealing variations in the frequency-dependent dielectric function $\varepsilon(\nu)$ or associated parameters through the transition.

The previous studies provide relatively modest SCO-induced changes in dielectric properties and have sought to use DFT calculations of the polarizabilities of isolated complexes to interpret the experimental $\varepsilon(T)$ data. The present article extends these studies to consider fully periodic hybrid DFT calculations of the variation in the dielectric tensor of the $Cs^+Fe^{2+}[Cr^{3+}(CN)_6]$ Prussian blue analogue (PBA, Figure I) through the hysteretic thermal SCO transition at $T_{1/2}(\uparrow)$ = 238 K and $T_{1/2}(\downarrow)$ = 211 K [8]. The SCO transition has also been found to be sensitive to the application of

hydrostatic pressure [9] and X-ray illumination [51]. This extended framework material is chosen as a case for which solid-state calculations are essential, given the difficulties in isolating a representative cluster suitable for molecular calculations. It has been the subject of previous theoretical studies [52,53], the most recent by one of the present authors, seeking to compute the free energies of the HS and LS states and $T_{1/2}$ by means of lattice dynamics calculations using hybrid density functionals [54]. The periodic approach offers the advantage that all relevant species, namely the $Fe[Cr(CN)_6]^-$ framework and Cs^+ counterions, are straightforwardly included. The 'clamped nuclei' (high frequency, purely electronic) and phonon contributions to the dielectric tensor are separately determined and each shown to be significant for both spin states. Note that DFT calculations of the polarizabilities of isolated molecules would encounter difficulties in accurately representing the full electrostatic and elastic environment encountered in SCO solids.

To the best of our knowledge, what follows represents the first solid-state calculations of the dielectric parameters of a SCO material. The results below yield a change in static dielectric constant $\Delta\varepsilon^0$ = +0.6 to +1.2 (varying with crystal axis and hybrid functional), a value that is significantly larger than those observed in the materials discussed above. Moreover, the dominant phonon contribution $\Delta\varepsilon^{\text{phon}}(\text{HS}-\text{LS})$ ($\Delta\varepsilon^{\text{phon}}$ hereafter) is, in turn, dominated by the Cs^+ counterion translational modes. Taken together with their structural and doping flexibility, this suggests that PBAs and other metal-organic frameworks may be a fruitful class of materials in which to search for SCO transitions occurring with large changes in dielectric parameters and other macroscopic properties. More generally, the design of SCO materials with desirable attributes has typically focused upon the selective modification of

intramolecular chemistry, e.g. by substitution or addition of groups. The present results show that intermolecular electrostatics, crystal packing and environment can all play equally important roles. For example, the large $\Delta\varepsilon^0$ value in $CsFe[Cr(CN)_6]$ arises due to the combination of the opposite charges borne by the Cs^+ and $Fe[Cr(CN)_6]^-$ sublattices, the facile displacements of the former ions within the structure, and the substantial volume expansion through the LS→HS transition.

II. Computational Methods and Dielectric Model

All of the present calculations are performed within the CRYSTAL09 code [55-62] using atomic basis sets comprising contractions of primitive Gaussian-type functions, and two distinct hybrid functionals combining Hartree-Fock (HF) and DFT exchange with a DFT correlation functional. The admixture of HF exchange in the functional is denoted as F_0, with values F_0=14 and 20% being used here, as supported by the results of a previous study [54]. All structures were fully geometry optimized (varying all cell parameters and atomic positions) prior to calculations of vibrational frequencies and dielectric tensors. The experimental cell volumes and optimized structures are presented in the Supplementary Material [63]. Calculations of the dielectric response of the HS and LS states proceed via the coupled-perturbed Kohn-Sham/Hartree-Fock theory for the clamped nuclei (high frequency) $\varepsilon_{ii}^{\infty}$ contribution [60-62], and by the combination of the computed atomic dynamical charge tensors [64] with the vibrational eigenvectors for the contribution of each normal mode. The frequency dependent $\varepsilon_{ii}(\nu)$ dielectric tensors are obtained within a damped harmonic oscillator model [64-66] as a sum over polar modes (n) of the form

$$\varepsilon_{ii}(\nu) = \varepsilon_{ii}^{\infty} + \sum_{n} \frac{f_{nii}\nu_n^2}{\nu_n^2 - \nu^2 - i\nu\gamma_n}, \quad (1)$$

where f_{nii} is the axis-dependent mode oscillator strength, and γ_n, the mode damping factor. The static ($\nu = 0$) dielectric tensor ε_{ii}^{0} is then straightforwardly obtained as the sum

$$\varepsilon_{ii}^{0} = \varepsilon_{ii}^{\infty} + \sum_{n} f_{nii} = \varepsilon_{ii}^{\infty} + \varepsilon_{ii}^{phon}, \quad (2)$$

of the clamped nuclei component with the sum of the oscillator strengths of the polar phonons active along the corresponding crystal axis. Note that the LS and HS state structures are cubic and tetragonal, respectively, leading to diagonal dielectric tensors in each case. The computational methods and theory of the model dielectric functions are fully described in the Supplementary Material [63].

III. Results and Discussion

Examining the computed results, first, the previous solid-state calculations [54] used the enthalpy difference between the constrained cubic (but volume relaxed) HS and the fully relaxed Jahn-Teller (JT) distorted HS geometries, ΔH_{JT}, as a measure of the tendency to form an orbital disordered state on the HS Fe^{2+} sublattice. In all cases, ΔH_{JT}, at approximately 0.2 kJ/mol or lower, was found to be lower than TS_{orb} for $T \geq T_{1/2}$, where $S_{orb} = R\ln(3)$ is the orbital entropy associated with the three degenerate $e_g^2 t_{2g}^4$ configurations in the octahedral HS Fe^{2+} cation, suggesting that orbital disorder is favored. This approach suffers from a number of limitations,

mainly that the representation of the constrained cubic and JT-distorted geometries within a primitive cell imposes an artificially high degree of coherency on the structure. Here, the energetics of distinct states of orbital order are considered, as represented within three supercells each containing two HS Fe^{2+} sites. Two distinct states of Fe^{2+} orbital occupation are considered for each supercell, presented along with the supercell expansions and orbital ordering enthalpy differences in Table I. It is clear that the enthalpy differences separating distinct states of orbital order are very small (all are less than 0.6 kJ/mol and of the same order of magnitude as ΔH_{JT} in the previous study) and remain consistent with the likely presence of orbital disorder in the HS state of this material. Thus, while the elastic interactions between HS↔LS Fe^{2+} sites are appreciable due to the large change in effective ionic radius through the SCO transition, the HS↔HS site interactions associated with distinct states of orbital occupation are much weaker due to the smaller structural changes splitting the t_{2g} orbital degeneracy. This is in keeping with the understanding that JT distortions associated with t_{2g} orbital degeneracy are typically rather weak, although this must clearly depend upon the strength and nature of metal-ligand π-bonding [67].

Examining optimized structures, it is found that, as in the previous DFT study [54], the present structural optimizations accurately reproduce the experimental increase in lattice constant $\Delta a(HS-LS)$ = +0.38 Å (denoted Δa hereafter) through the LS→HS transition [8]. An average over functionals yields Δa = +0.418 Å and $\Delta c(HS-LS)$ = +0.427 Å (denoted Δc hereafter) with respect to the tetragonal HS cell, and Δa_{aver} = +0.421 Å assuming an axial average consistent with HS state orbital disorder. Individual bond lengths are very similar to those presented in the earlier study [54]. Note that the $z^2(\uparrow), xz(\uparrow), yz(\uparrow), x^2-y^2(\uparrow), xy(\uparrow\downarrow)$ orbital occupation is selected

hereafter for the HS Fe^{2+} state, leading to symmetry-equivalent x- and y-axes, and a symmetry-distinct z-axis.

The clamped nuclei (or high frequency) dielectric tensor contributions, $\varepsilon_{ii}^{\infty}$, are computed by solution of the CPKS/HF equations [60-62] in the HS and LS state optimized geometries discussed above. The results, shown in Table II, reveal significantly higher values in the LS state, particularly for the $\varepsilon_{zz}^{\infty}$ component oriented along the HS cell tetragonal axis, with a mean value $\Delta\varepsilon^{\infty}(\mathrm{HS}-\mathrm{LS}) = -0.481$ averaged over axes and functionals. This is the opposite of the trend discussed above, namely that the majority of SCO materials show positive $\Delta\varepsilon$ values. Note, however, that it is the static dielectric constant difference, $\Delta\varepsilon^{0}$, rather than the clamped nuclei difference, $\Delta\varepsilon^{\infty}$, that should be compared with experimental DDS data obtained at frequencies $\nu = 10^2 - 10^7$ Hz lying well below the vibrational resonances; we return to this point later. It is also useful to compare the directly-calculated polarizabilities, α_{ii}, along the crystal axes, as also shown in Table II, noting that $\varepsilon_{ii}^{\infty} = 1 + (4\pi\alpha_{ii}/\Omega)$. Here, a mean value $\Delta\alpha(\mathrm{HS}-\mathrm{LS})$ = -48.71 $bohr^3$ averaged over axes and functionals is obtained for the primitive cells, factor $4\pi/\Omega$ being approximately 0.0059 and 0.0066 $bohr^{-3}$ in the HS and LS states, respectively. Noting that the refractive index may be defined as $n = \sqrt{\varepsilon^{\infty}}$, it is evident that the crystal is notionally birefringent in the HS state, given the presence of disparate $\varepsilon_{xx}^{\infty} = \varepsilon_{yy}^{\infty}$ and $\varepsilon_{zz}^{\infty}$ values. However, likely Fe^{2+} orbital disorder in the HS state would result in a monorefringent material averaged over length scales longer than a few unit cells.

A symmetry analysis of the normal modes anticipated in the LS and HS primitive cells is a useful preliminary. For the primitive tetragonal HS cell, the modes at the reciprocal space Γ-point comprise

$$\Gamma_{optical} = 4\times A_1(1) + 4\times A_2(1) + 2\times B_1(1) + 8\times B_2(1) + 12\times E(2),$$

and $$\Gamma_{acoustic} = 1\times E(2) + 1\times B_2(1),$$

with symmetry degeneracies in parentheses. Twelve doubly-degenerate E-symmetry optical modes contribute to $\varepsilon_{xx}^{phon} = \varepsilon_{yy}^{phon}$, and eight singly-degenerate B_2-symmetry optical modes to ε_{zz}^{phon}. The optical modes have finite frequencies at the Γ-point, while the acoustic modes correspond to uniform translations of all atoms in the cell and should have zero frequencies (or, in practice, near-zero frequencies due to numerical imprecision) at the Γ-point [68]. Meanwhile, for the primitive cubic LS cell, the modes comprise

$$\Gamma_{optical} = 2\times A(1) + 2\times E(2) + 4\times F_1(3) + 8\times F_2(3),$$

and $$\Gamma_{acoustic} = 1\times F_2(3),$$

where eight triply-degenerate F_2-symmetry optical modes contribute to $\varepsilon_{xx}^{phon} = \varepsilon_{yy}^{phon} = \varepsilon_{zz}^{phon}$.

The atomic dynamical charges in the HS and LS structures are very similar to those reported in the previous study [54] and are presented in the Supplementary Material [63]. The individual mode contributions to ε^{phon} arising in the $F_0 = 14\%$ hybrid are

presented in Table III. The F_0 = 20% results are quantitatively similar; mode frequencies and oscillator strengths for all spin states in both hybrid functionals are presented in the Supplementary Material [63]. Only the dominant mode contributions are shown (i.e. those each contributing more than 1 % of ε^{phon}), reducing their numbers to seven E- and four B_2-symmetry modes in the HS state, and three F_2-symmetry modes in the LS state. Interestingly, it emerges that the dominant part of ε^{phon} in both the HS and LS state arises due to low frequency Cs^+ translational modes. The other significantly-contributing modes all involve either tetrahedral or pyramidal FeN_4/CrC_4 deformations along the respective crystal axis in combination with Cr−C and Fe−N bond stretches. More specifically, in the F_0 = 14% hybrid, the Cs^+ translations contribute 70, 60 and 76 % of ε^{phon} for the E- and B_2-symmetry modes in the HS state and the F-symmetry modes in the LS state, respectively, with similar percentage contributions in the F_0 = 20% hybrid.

The relative contributions of ε_{ii}^{phon} and $\varepsilon_{ii}^{\infty}$ to the static dielectric tensors ε_{ii}^{0} may be compared in Table II. In both functionals, and along all axes, the phonon contribution suffices to reverse the order of dielectric tensor elements relative to the clamped nuclei contribution, so that $\Delta\varepsilon^0$ is always positive with a mean value of +0.831 averaged over all axes and functionals. Thus, the sign of $\Delta\varepsilon^0$ in $Cs^+Fe^{2+}[Cr^{3+}(CN)_6]$ is now in agreement with the trend evident in other SCO materials, as discussed above. It is likely that the phonon contribution to $\Delta\varepsilon^0$ may be significant in other SCO materials and should routinely be considered in future studies. Also of interest is the finding that $\Delta\varepsilon^0$ in the present material is significantly larger than the highest of the

experimental values presented above for other SCO compounds, namely $\Delta\varepsilon = +0.3$ for the $[Fe(NH_2trz)_3](NO_3)_2$ (trz = triazole) complex [36].

Decomposing $\Delta\varepsilon^{phon}$, it again emerges that the Cs^+ translational modes are the dominant contributors, comprising 61 % of the total averaged over all axes and functionals. This is likely due to the fact that the Cs^+ cations are loosely bound in the structure, which, together with their high mass, yields very low vibrational frequencies. These low energy modes provide a facile means by which to polarize the material in response to a slowly varying or static electric field. Furthermore, they are expected to be very sensitive to the significant cell volume change associated with the SCO transition, as borne out by the large increases in oscillator strength through the LS→HS transition shown in Table III. More explicitly, for the F_0 = 14% hybrid, while the effective masses (μ) of the Cs^+ translational modes at ν = 38.3 and 41.4 cm^{-1} in the HS state, and 62.3 cm^{-1} in the LS state, are all very similar at μ = 43.8, 43.7 and 44.5 amu per mode, respectively, the mode force constants (k) vary significantly through the SCO transition, yielding values k = 3.78, 4.41 and 10.18 Nm^{-1}, respectively. Similar results are obtained with the F_0 = 20% hybrid functional. Taking all of the above together, the selective substitution of Cs^+ by singly-charged M^+ counterions with different ionic radii, or by doubly-charged species and an appropriate number of vacancies (V), i.e. $Cs^+ \rightarrow M^{2+} + V_{Cs}^-$, seem reasonable strategies to alter $T_{1/2}(\uparrow)$, $T_{1/2}(\downarrow)$ and $\Delta\varepsilon^0$. Furthermore, the isotropic bonding and doping flexibility of the PBAs and related metal-organic frameworks make them an ideal class of materials in which to search for SCO compounds displaying useful changes in macroscopic properties through the transition. Given the findings above, it

is clear that materials containing weakly bound counterions may be of particular interest.

Finally, Figure II(a) and (b) show the real (Re) and imaginary (Im) parts, respectively, of the complex dielectric function $\varepsilon_{ii}(\nu)$, computed as detailed above, using an intermediate damping factor $\gamma_n = \gamma = 10$ cm^{-1} for all polar modes. The $\varepsilon(\nu)$ functions obtained for a broader range of damping factors are presented in the Supplementary Material [63]. Note that first principles calculations of the phonon damping factors are not straightforward, given that they involve higher derivatives of the lattice potential energy with respect to atomic displacements. The $\varepsilon_{xx}(\nu) = \varepsilon_{yy}(\nu)$ and $\varepsilon_{zz}(\nu)$ contributions are presented separately and in an averaged form $\varepsilon_{aver}(\nu) = [2\varepsilon_{xx}(\nu) + \varepsilon_{zz}(\nu)]/3$ for the tetragonal HS structure, where the latter seeks to account for possibile Fe^{2+} orbital disorder. Interestingly, $\mathrm{Re}[\varepsilon_{zz}(\nu)]$ for the HS state falls to negative values in three frequency ranges ν = 210−235, 377−396 and 473−482 cm^{-1}, and similarly, $\mathrm{Re}[\varepsilon_{aver}(\nu)]$, in two ranges ν = 388−393 and 479−480 cm^{-1}. Negative values of $\mathrm{Re}[\varepsilon(\nu)]$ are associated with complete reflection of incident radiation, leading to the appearance of 'reststrahlen' bands in the IR reflectance spectrum [69]. Note, however, that the precise locations and widths of the reststrahlen bands will, in general, be strongly dependent on the mode damping factor(s) applied in the calculation of $\varepsilon(\nu)$, and so the present calculations can only offer a guide to their likely locations. No such reflection bands are predicted in the LS state spectra, although this again depends upon the damping factor(s) applied. In addition to IR reflectance spectroscopy, the theoretical determination of $\varepsilon(\nu)$ will aid the interpretation of terahertz spectroscopy and spectroscopic ellipsometry data [49,50] in the present and in other SCO materials.

IV. Conclusions

In conclusion, the present study computes a significantly larger variation in the dielectric parameters of the $CsFe[Cr(CN)_6]$ PBA through the thermal SCO transition than has been observed in other SCO materials [36-39]. The current approach is based upon solid-state hybrid DFT calculations, and includes, we believe for the first time, a separate account of the clamped nuclei and phonon contributions to the dielectric tensors of the HS and LS states. The latter contribution is found to be non-negligible in all cases, and leads to the observation that, while the clamped nuclei term $\Delta\varepsilon_{ii}^{\infty}(\mathrm{HS}-\mathrm{LS})$ is negative for all axes and functionals, the difference in static dielectric constants, $\Delta\varepsilon_{ii}^{0}(\mathrm{HS}-\mathrm{LS}) = \Delta\varepsilon_{ii}^{\infty}(\mathrm{HS}-\mathrm{LS}) + \Delta\varepsilon_{ii}^{\mathrm{phon}}(\mathrm{HS}-\mathrm{LS})$, is always positive, consistent with the majority of experimental data for a range of SCO materials. Moreover, the phonon contribution $\Delta\varepsilon_{ii}^{\mathrm{phon}}(\mathrm{HS}-\mathrm{LS})$ dominates over $\Delta\varepsilon_{ii}^{\infty}(\mathrm{HS}-\mathrm{LS})$ in determining $\Delta\varepsilon_{ii}^{0}(\mathrm{HS}-\mathrm{LS})$, and is in turn dominated by modes involving the translational motions of the Cs^+ counterions within the cubic voids of the $Fe[Cr(CN)_6]^-$ framework. The large contribution of the Cs^+ counterions to $\Delta\varepsilon^{0}(\mathrm{HS}-\mathrm{LS})$ is consistent with their relatively open environments and weak bonding, permitting large displacements in response to applied electric fields. This finding opens up the possibility of the selective substitution of Cs^+ with other M^+ species, or with $M^{2+} + V_{Cs}^{-}$ (where V indicates a site vacancy), as a means to alter not just $T_{1/2}(\uparrow)$ and $T_{1/2}(\downarrow)$, but also $\Delta\varepsilon_{ii}^{0}(\mathrm{HS}-\mathrm{LS})$ in this system. More generally, the present results suggest a potentially fruitful strategy in the search for new SCO materials displaying useful variations in dielectric response and other macroscopic properties, this being to focus upon solids bearing oppositely charged sublattices, one

of which is relatively loosely and isotropically bound in the framework delineated by the other. Furthermore, it is clear that the SCO-active Fe^{2+} (or other TM) species must be fully integrated into the framework in order to realize a significant volume change through the transition.

V. Acknowledgements

The authors acknowledge the support of the UK EPSRC under grant number EP/K012940/1. Research carried out (in whole or in part) at the Center for Functional Nanomaterials, Brookhaven National Laboratory, which is supported by the U.S. Department of Energy, Office of Basic Energy Sciences, under Contract No. DE-AC02-98CH10886.

VI. References

[1] M. A. Halcrow (Ed.), *Spin Crossover Materials: Properties and Applications*, Wiley-Blackwell (2013)

[2] H. Paulsen, V. Schünemann and J. A. Wolny, Eur. J. Inorg. Chem, 628 (2013)

[3] P. Gütlich, Struct. Bonding **44**, 83 (1981);

[4] P. Gütlich, A. Hauser and H. Spiering, Angew. Chem., Int. Ed. Engl. **33**, 2024 (1994)

[5] E. König, Struct. Bonding **76**, 51 (1991)

[6] O. Kahn and C. J. Martinez, Science **279**, 44 (1998)

[7] A. Bousseksou, K. Boukheddaden, M. Goiran, C. Conséjo, M.-L. Boillot and J.-P. Tuchagues, Phys. Rev. B **65**, 172412 (2002)

[8] W. Kosaka, K. Nomura, K. Hashimoto and S. Ohkoshi, J. Am. Chem. Soc. **127**, 8590 (2005)

[9] D. Papanikolaou, W. Kosaka, S. Margadonna, H. Kagi, S. Ohkoshi and K. Prassides, J. Phys. Chem. C **111**, 8086 (2007)

[10] P. D. Southon, L. Liu, E. A. Fellows, D. J. Price, G. J. Halder, K. W. Chapman, B. Moubaraki, K. S. Murray, J.-F. Létard and C. J. Kepert, J. Am. Chem. Soc. **131**, 10998 (2009)

[11] M. Sorai and S. Seki, J. Phys. Chem. Solids **35**, 555 (1974)

[12] N. Willenbacher and H. Spiering, J. Phys. C **21**, 1423 (1988)

[13] J. Wajnflasz, Phys. Status Solidi **40**, 537 (1970)

[14] C. P. Slichter and H. G. Drickamer, J. Chem. Phys. **56**, 2142 (1972)

[15] S. Hayami, Z.-z. Gu, H. Yoshiki, A. Fujishima and O. Sato, J. Am. Chem. Soc. **123**, 11644 (2001)

[16] B. Weber, E. S. Kaps, J. Obel, K. Achterhold and F. G. Parak, Inorg. Chem. **47**, 10779 (2008)

[17] B. Weber, W. Bauer and J. Obel, Angew. Chem. Int. Ed. **47**, 10098 (2008)

[18] D.-Y. Wu, O. Sato, Y. Einaga and C.-Y. Duan, Angew. Chem. **121**, 1503 (2008)

[19] J. A. Real, I. Castro, A. Bousseksou, M. Verdaguer, R. Burriel, M. Castro, J. Linares and F. Varret, Inorg. Chem. **36**, 455 (1997)

[20] K. Nakano, S. Kawata, K. Yoneda, A. Fuyuhiro, T. Yagi, S. Nasu, S. Morimoto and S. Kaizaki, Chem. Commun. 2892 (2004)

[21] R. Boca, M. Boca, H. Ehrenberg, H. Fuess, W. Linert, F. Renz and I. Svoboda, Chem. Phys. **293**, 375 (2003)

[22] P. Guionneau, M. Marchivie, G. Bravic, J.-F. Létard and D. Chasseau, Topics. Curr. Chem. **234**, 97 (2004)

[23] P. Guionneau, J.-F. Létard, D. S. Yufit, D. Chasseau, G. Bravic, A. E. Goeta, J. A. K. Howard and O. Kahn, J. Mater. Chem. **9**, 985 (1999)

[24] V. A. Money, J. Elhaïk, I. R. Evans, M. A. Halcrow and J. A. K. Howard, Dalton. Trans. 65 (2004)

[25] M. A. Halcrow, Chem. Soc. Rev. **40**, 4119 (2011)

[26] J. A. Wolny, R. Diller and V. Schünemann, Eur. J. Inorg. Chem, 2635 (2012)

[27] G. Molnár, V. Niel, A. B. Gaspar, J.-A. Real, A. Zwick, A. Bousseksou and J. J. McGarvey, J. Phys. Chem. B **106**, 9701 (2002)

[28] H. Paulsen, R. Benda, C. Herta, V. Schünemann, A. I. Chumakov, L. Duelund, H. Winkler, H. Toftlund and A. X. Trautwein, Phys. Rev. Lett. **86**, 1351 (2001)

[29] G. J. Halder, C. J. Kepert, B. Moubaraki, K. S. Murray and J. D. Cashion, Science **298**, 1762 (2002)

[30] J. A. Real, E. Andrés, M. C. Muñoz, M. Julve, T. Granier, A. Bousseksou and F. Varret, Science **268**, 265 (1995)

[31] O. Sato, Acc. Chem. Res. **36**, 692 (2003)

[32] L. G. Lavrenova and O. G. Shakirova, Eur. J. Inorg. Chem. 670 (2013)

[33] K. Takahashi, H.-B. Cui, Y. Okano, H. Kobayashi, H. Mori, H. Tajima, Y. Einaga and O. Sato, J. Am. Chem. Soc. **130**, 6688 (2008)

[34] C. Faulmann, K. Jacob, S. Dorbes, S. Lampert, I. Malfant, M.-L. Doublet, L. Valade and J. A. Real, Inorg. Chem. **46**, 8548 (2007)

[35] M. Nihei, N. Takahashi, H. Nishikawa and H. Oshio, Dalton Trans. **40**, 2154 (2011)

[36] A. Bousseksou, G. Molnár, P. Demont and J. Menegotto, J. Mater. Chem. **13**, 2069 (2003)

[37] T. Guillon, S. Bonhommeau, J. S. Costa, A. Zwick, J.-F. Létard, P. Demont, G. Molnár and A. Bousseksou, Phys. Stat. Sol. (a) **203**, 2974 (2006)

[38] S. Bonhommeau, T. Guillon, L. M. L. Daku, P. Demont, J. S. Costa, J.-F. Létard, G. Molnár and A. Bousseksou, Angew. Chem. Int. Ed. **45**, 1625 (2006)

[39] M. Nakano, G. Matsubayashi and T. Matsuo, Phys. Rev. B **66**, 212412 (2002)

[40] F. Prins, M Monrabal-Capilla, E. A. Osorio, E. Coronado and H. S. J. van der Sant, Adv. Mater. **23**, 1545 (2011)

[41] G. Molnár, S. Cobo, J. A. Real, F. Carcenac, E. Daran, C. Vieu and A. Bousseksou, Adv. Mater. **19**, 2163 (2007)

[42] C. Bartual-Murgui, L. Salmon, A. Akou, N. A. Ortega-Villar, H. J. Shepherd, M. C. Muñoz, G. Molnár, J. A. Real and A. Bousseksou, Chem. Eur. J. **18**, 507 (2012)

[43] P. Durand, S. Pillet, E.-E. Bendeif, C. Carteret, M. Bouazaoui, H. E. Hamzaoui, B. Capoen, L. Salmon, S. Hébert, J. Ghanbaja, L. Aranda and D. Schaniel, J. Mater. Chem. C **1**, 1933 (2013)

[44] T. D. Roberts, F. Tuna, T. L. Malkin, C. A. Kilner and M. A. Halcrow, Chem. Sci. **3**, 349 (2012)

[45] J.-F. Létard, G. Chastanet, P. Guionneau and C. Desplanches, in *Spin Crossover Materials: Properties and Applications*, M. A. Halcrow Ed., Wiley-Blackwell (2013)

[46] F. Varret, K. Boukheddaden, G. Chastanet, N. Paradis and J.-F. Létard, Eur. J. Inorg. Chem., 763 (2013)

[47] M. Clemente-León, E. Coronado, M. López-Jordà, J. C. Waerenborgh, C. Desplanches, H. Wang, J.-F. Létard, A. Hauser and A. Tissot, J. Am. Chem. Soc. **135**, 8655 (2013)

[48] A. Bousseksou, C. Vieu, J.-F. Létard, P. Demont, J.-P. Tuchagues, L. Malaquin, J. Menegotto, L. Salmon, patent EP1430552 (2004)

[49] P. Mounaix, N. Lascoux, J. Degert, E. Freysz, A. Kobayashi, N. Daro and J.-F. Létard, Appl. Phys. Lett. **87**, 244103 (2005)

[50] K. Boukheddaden, E. D. Loutete-Dangui, M. Koubaa and C. Eypert, Phys. Stat. Sol. C **5**, 1003 (2008)

[51] D. Papanikolaou, S. Margadonna, W. Kosaka, S. Ohkoshi, M. Brunelli, and K. Prassides, J. Am. Chem. Soc. **128**, 8358 (2006)

[52] B. Le Guennic, S. Borshch, and V. Robert, Inorg. Chem. **46**, 11106 (2007)

[53] J. C. Wojdeł, I. P. R. Moreira, and F. Illas, J. Chem. Phys. **130**, 014702 (2009)

[54] D. S. Middlemiss, D. Portinari, C. P. Grey, C. A. Morrison and C. C. Wilson, Phys. Rev. B **81**, 184410 (2010)

[55] R. Dovesi, R. Orlando, B. Civalleri, C. Roetti, V. R. Saunders and C. M. Zicovich-Wilson, Z. Kristallogr. **220**, 571 (2005)

[56] R. Dovesi, V. R. Saunders, C. Roetti, R. Orlando, C. M. Zicovich-Wilson, F. Pascale, B. Civalleri, K. Doll, N. M. Harrison, I. J. Bush, Ph. D'Arco, M. Llunell CRYSTAL09 User's Manual, University of Torino (2009)

[57] F. Pascale, C.M. Zicovich-Wilson, F. Lopez, B. Civalleri, R. Orlando and R. Dovesi, J. Comput. Chem. **25**, 888 (2004)

[58] C.M. Zicovich-Wilson, F. Pascale, C. Roetti, V.R. Saunders, R. Orlando and R. Dovesi, J. Comput. Chem. **25**, 1873 (2004)

[59] C. M. Zicovich-Wilson, R. Dovesi, and V. R. Saunders, J. Chem. Phys. **115**, 9708 (2001)

[60] M. Ferrero, M. Rérat, R. Orlando and R. Dovesi, J. Comput. Chem. **29**, 1450 (2008)

[61] M. Ferrero, M. Rérat, R. Orlando and R. Dovesi, J. Chem. Phys. **128**, 014110 (2008)

[62] M. Ferrero, M. Rérat, B. Kirtman and R. Dovesi, J. Chem. Phys. **129**, 244110 (2008)

[63] See Supplementary Material Document No._____ for detailed computational methodology and theory of dielectric response, optimized and experimental structures, mode frequencies and oscillator strengths, scalar dynamical charges, mode eigenvectors and tabulated dielectric functions computed with alternative damping factors. For information on Supplementary Material, see http://www.aip.org/pubservs/epaps.html

[64] M. Born and K. Huang, *Dynamical Theory of Crystal Lattices*, Clarendon Press, Oxford (1954)

[65] M. De La Pierre, R. Orlando, L. Maschio, K. Doll, P. Ugliengo and R. Dovesi, J. Comput. Chem **32**, 1775 (2011)

[66] Y. Noël, M. De La Pierre, L. Maschio, M. Rérat, C. M. Zicovich-Wilson and R. Dovesi, Int. J. Quantum Chem. **112**, 2098 (2012)

[67] R. J. Deeth, A. E. Anastasi and K. Randall, Dalton Trans. 6007 (2009)

[68] M. T. Dove, *Introduction to Lattice Dynamics*, Cambridge University Press, Cambridge (1993)

[69] M. Fox, *Optical Properties of Solids*, Oxford University Press, Oxford (2010)

Tables

Supercell	ΔH(kJ/mol)	
	$F_0 = 14\%$	$F_0 = 20\%$
1[a]	+0.20	+0.54
2[b]	+0.33	+0.54
3[c]	−0.04	+0.15

[a] $\mathbf{a}_{scell}=\mathbf{b}_{prim}+\mathbf{c}_{prim}$, $\mathbf{b}_{scell}=\mathbf{a}_{prim}+\mathbf{c}_{prim}$ and $\mathbf{c}_{scell}=\mathbf{a}_{prim}+\mathbf{b}_{prim}$

[b] $\mathbf{a}_{scell}=2\mathbf{a}_{prim}$, $\mathbf{b}_{scell}=\mathbf{b}_{prim}$ and $\mathbf{c}_{scell}=\mathbf{c}_{prim}$

[c] $\mathbf{a}_{scell}=\mathbf{a}_{prim}+\mathbf{b}_{prim}-\mathbf{c}_{prim}$, $\mathbf{b}_{scell}=\mathbf{c}_{prim}$ and $\mathbf{c}_{scell}=\mathbf{a}_{prim}-\mathbf{b}_{prim}$

Table I. The enthalpy difference (kJ/mol) separating fully relaxed HS Fe^{2+} orbital configurations, $\Delta H = H[Fe_A(C_1) + Fe_B(C_1)] - H[Fe_A(C_1) + Fe_B(C_2)]$ as represented in three structurally-distinct double formula unit supercells each containing two Fe sites denoted Fe_A and Fe_B. Orbital configurations (C) at each HS Fe site are defined as C_1=$z^2(\uparrow), xz(\uparrow), yz(\uparrow), x^2-y^2(\uparrow), xy(\uparrow\downarrow)$ and C_2=$z^2(\uparrow), xz(\uparrow\downarrow), yz(\uparrow), x^2-y^2(\uparrow), xy(\uparrow)$. The supercells (scell) are defined in terms of the lattice vectors of the rhombohedral (or near-rhombohedral in the case of the tetragonal HS state) primitive (prim) cells.

		F_0 = 14%			F_0 = 20%		
		xx	yy	zz	xx	yy	zz
HS	ε^{∞}	2.448	2.448	2.159	2.218	2.218	2.083
	α	246.90	246.90	197.69	208.48	208.48	185.37
	$\varepsilon^{\mathrm{phon}}$	1.835	1.835	2.558	1.945	1.945	2.565
	ε^{0}	4.283	4.283	4.717	4.163	4.163	4.648
LS	ε^{∞}	2.889	2.889	2.889	2.597	2.597	2.597
	α	285.50	285.50	285.50	243.20	243.20	243.20
	$\varepsilon^{\mathrm{phon}}$	0.798	0.798	0.798	0.807	0.807	0.807
	ε^{0}	3.687	3.687	3.687	3.404	3.404	3.404
$\Delta\varepsilon^{\infty}(\mathrm{HS}-\mathrm{LS})$		-0.441	-0.441	-0.730	-0.379	-0.379	-0.514
$\Delta\varepsilon^{\mathrm{phon}}(\mathrm{HS}-\mathrm{LS})$		+1.037	+1.037	+1.760	+1.138	+1.138	+1.758
$\Delta\varepsilon^{0}(\mathrm{HS}-\mathrm{LS})$		+0.596	+0.596	+1.030	+0.759	+0.759	+1.244

Table II. The clamped nuclei (ε^{∞}), static (ε^{0}) and phonon contribution ($\varepsilon^{\mathrm{phon}} = \varepsilon^{0} - \varepsilon^{\infty}$) to the diagonal dielectric tensors, and the clamped nuclei polarizabilities (α, bohr^3) computed by solution of the CPKS/HF equations and by lattice dynamics calculations in the HS and LS states for the F_0=14% and 20% hybrid functionals. The respective HS−LS differences are shown below.

(a)

ν	Irrep.	f_{xx}/f_{yy} (%)	Assignment
41.4	E	1.275 (69.5)	Cs translation (x/y)
162.2	E	0.062 (3.4)	FeN_4/CrC_4 OOP tetra. def. (x/y)
206.8	E	0.079 (4.3)	FeN_4/CrC_4 OOP pyra. def. + ν_{Cr-C} + ν_{Fe-N} (x/y)
243.9	E	0.154 (8.4)	FeN_4/CrC_4 OOP pyra. def. (x/y)
373.3	E	0.079 (4.3)	FeN_4/CrC_4 OOP tetra. def. + ν_{Cr-C} + ν_{Fe-N} (x/y)
386.5	E	0.092 (5.0)	FeN_4/CrC_4 OOP pyra. def. + ν_{Cr-C} + ν_{Fe-N} (x/y)
474.6	E	0.084 (4.6)	FeN_4/CrC_4 OOP pyra. def. + ν_{Cr-C} + ν_{Fe-N} (x/y)

(b)

ν	Irrep.	f_{zz} (%)	Assignment
38.3	B_2	1.533 (59.9)	Cs translation (z)
209.2	B_2	0.645 (25.2)	FeN_4/CrC_4 OOP pyra. def. + ν_{Cr-C} + ν_{Fe-N} (z)
375.9	B_2	0.259 (10.1)	FeN_4/CrC_4 OOP pyra. def. + ν_{Cr-C} + ν_{Fe-N} (z)
470.6	B_2	0.089 (3.5)	FeN_4/CrC_4 OOP pyra. def. + ν_{Cr-C} + ν_{Fe-N} (z)

(c)

ν	Irrep.	$f_{xx}/f_{yy}/f_{zz}$ (%)	Assignment
62.3	F_2	0.604 (75.6)	Cs translation (x/y/z)
254.8	F_2	0.083 (10.4)	FeN_4/CrC_4 OOP pyra. def. + ν_{Cr-C} + ν_{Fe-N} (x/y/z)
493.8	F_2	0.101 (12.7)	FeN_4/CrC_4 OOP pyra. def. + ν_{Cr-C} + ν_{Fe-N} (x/y/z)

Table III. The frequencies (ν, cm^{-1}), irreducible representation (Irrep.), oscillator strengths (f_{ii}, percentage of ε_{ii}^{phon} in parentheses) and mode assignment (OOP = out-of-plane, tetra. = tetrahedral, pyra. = pyramidal, def. = deformation and ν = stretch) of the dominant modes contributing to **(a)** $\varepsilon_{xx}^{phon} = \varepsilon_{yy}^{phon}$; **(b)** ε_{zz}^{phon} in the HS state; and **(c)** $\varepsilon_{xx}^{phon} = \varepsilon_{yy}^{phon} = \varepsilon_{zz}^{phon}$ in the LS state, all for the F_0=14% hybrid functional.

Figures

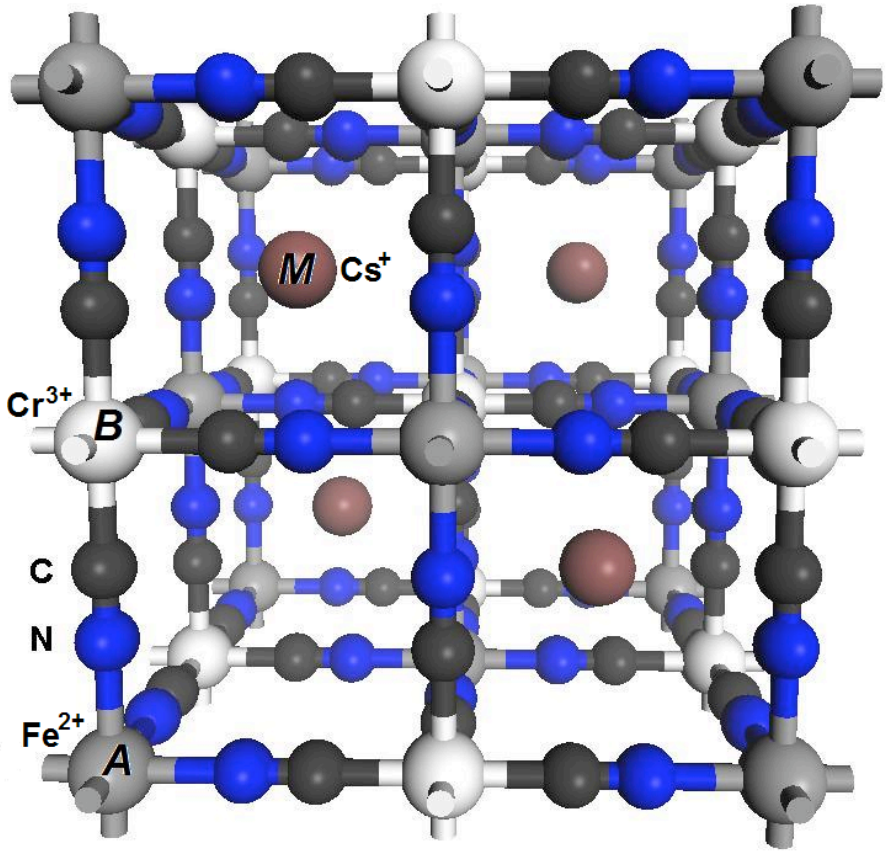

Figure I. The conventional crystallographic cell of the $Cs^{+}Fe^{2+}[Cr^{3+}(CN)_6]$ Prussian blue analogue.

(a)

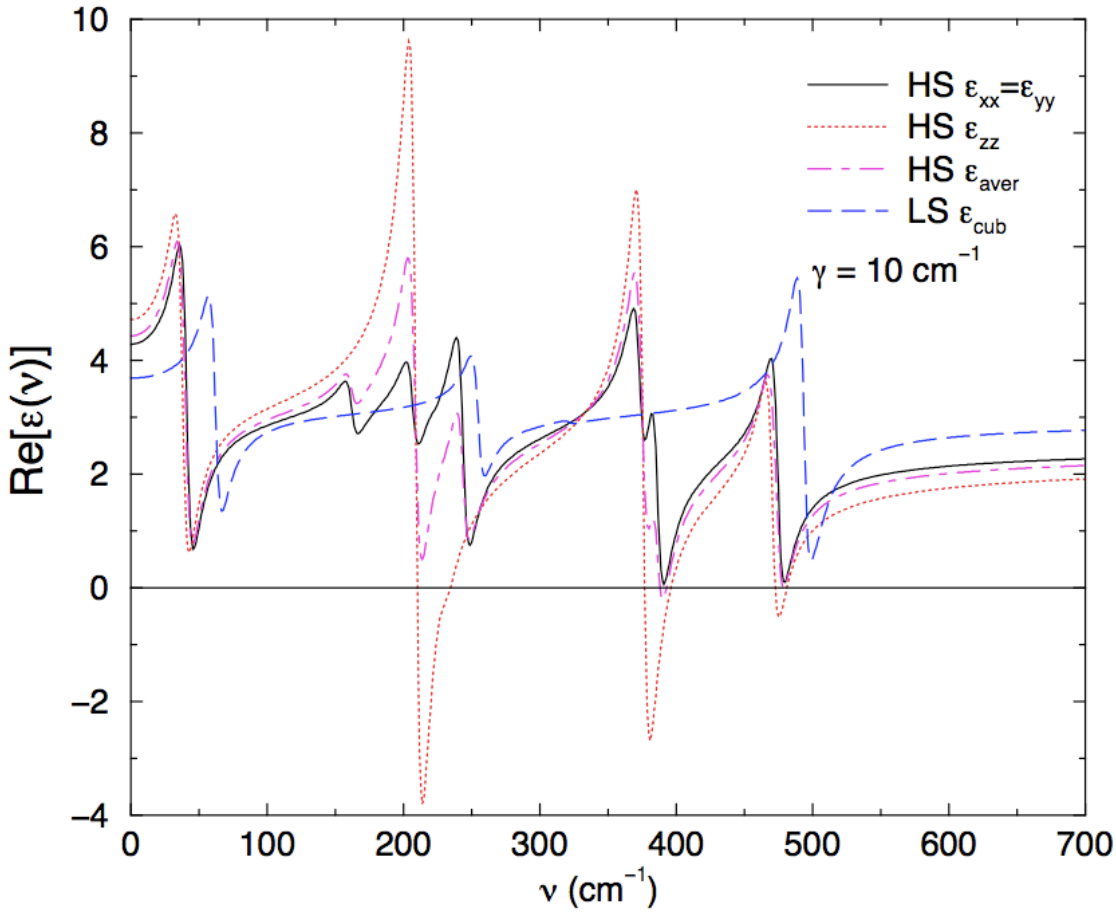
HS $\varepsilon_{xx}=\varepsilon_{yy}$
HS ε_{zz}
HS ε_{aver}
LS ε_{cub}
γ = 10 cm^{-1}
Re[$\varepsilon(\nu)$]
ν (cm^{-1})
10
8
6
4
2
0
−2
−4
0
100
200
300
400
500
600
700

(b)

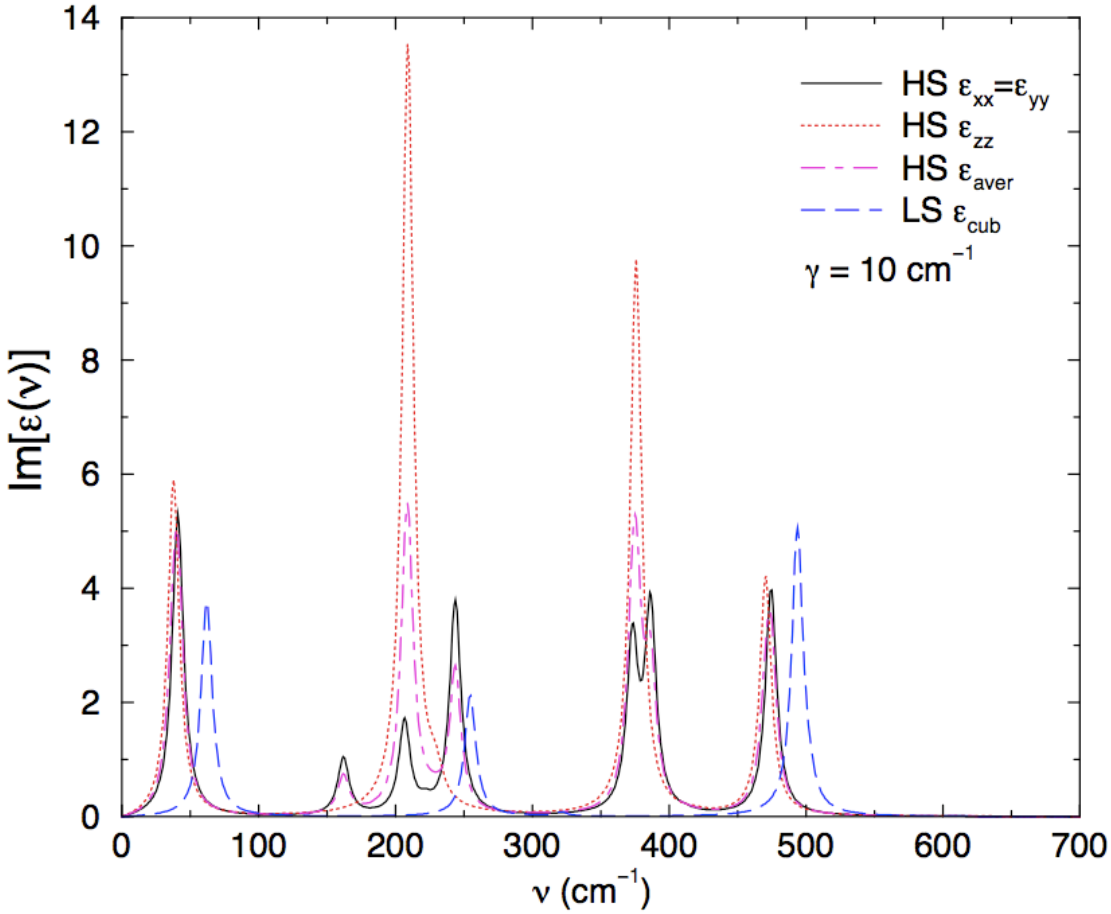

Figure II. The **(a)** real (Re) and **(b)** imaginary (Im) parts of the frequency-dependent dielectric tensor $\varepsilon_{ii}(\nu)$ obtained from the HS and LS state phonon frequencies and oscillator strengths in the F_0=14% hybrid functional. Separate $\varepsilon_{xx}(\nu) = \varepsilon_{yy}(\nu)$ and $\varepsilon_{zz}(\nu)$ components and axial average $\varepsilon_{aver}(\nu) = [2\varepsilon_{xx}(\nu) + \varepsilon_{zz}(\nu)]/3$ are shown for the tetragonal HS state, while a single $\varepsilon_{cub}(\nu) = \varepsilon_{xx}(\nu) = \varepsilon_{yy}(\nu) = \varepsilon_{zz}(\nu)$ tensor element is obtained for the cubic LS form. The damping factor γ was set to 10 cm^{-1} for all active modes. Note that the chosen frequency range excludes modes at 2216.4 and 2230.5 cm^{-1} in the HS state, and a mode at 2220.8 cm^{-1} in the LS state, but all of these modes have very low oscillator strengths $f < 0.005$.